Supplementary information

Comprehensive Study to Design Advanced Metal-carbid@Garaphene and Metal-carbide@FeO_x Nanoparticles with Tunable Structure by the Laser Ablation in liquid

Fatemeh Davodi [1], Elisabeth Mühlhausen [2], Daniel Settipani [1], Eeva-Leena Rautama [1], Ari-Pekka Honkanen [3], Simo Huotari [3], Galina Marzun [2], Pekka Taskinen [4], Tanja Kallio *[1]

[1] F. Davodi, D. Settipani, Dr. E. Rautama, Prof. T. Kallio
Electrochemical Energy Conversion Group, Department of Chemistry and Materials Science, School of Chemical Engineering, Aalto University, P.O. Box 16100, FI-00076 Aalto, Finland
Email: fatemeh.davodi@aalto.fi, tanja.kallio@aalto.fi

[2] E. Mühlhausen, Dr. G. Marzun
University of Duisburg-Essen, Technical Chemistry I and Center for Nanointegration Duisburg-Essen (CENIDE), Universitätsstr. 7, 45141 Essen, Germany

[3] Prof. S. Huotari, A. Honkanen
Department of Physics, University of Helsinki PO Box 64, FI–00014 Helsinki, Finland

[4] Prof. P. Taskinen
Department of Chemical and Metallurgical Engineering, School of Chemical Engineering, Aalto University, P.O. Box 16100, FI-00076 Aalto, Finland

Synthesis and characterization

Synthesis process of NiFe nanoparticles. The preparation of NiFe@UTG nanoparticles followed previous reports. [1] Briefly, NiFe NPs were synthesized by ultrashort-pulsed laser ablation in liquids as a facile technique for the synthesis of NPs described in detail elsewhere.[1] For this process an Nd: YAG laser (Ekspla, Atlantic) with a fundamental wavelength of 1064 nm, a pulse duration of 10 ps and a repetition rate of 100 kHz were used. A scanner (SCANcube10, Scanlab) moved the laser beam in a spiral pattern, and it was focused on the target with an f-theta lens (focal lens of 100 mm). The actual pulse energy applied, after the scanner and all optics, was 95 µJ. For synthesizing the NPs, a $Ni_{80}Fe_{20}$ (80%-20%, Sekels) was placed in a self-constructed stirred 100 mL aluminium batch chamber. The chamber was filled with acetone (analytical reagent grade, Fisher Chemical) and the ablation was carried out for 20 minutes. The collected colloid was used for further processing and analysis. To adjust the concentration, the solvent was evaporated at ambient temperature and pressure.

All other samples were synthesized with the same procedure with either different laser type (nano-second laser) or in different solutions in including ethanol, toluene and water or with different metal targets such as Ni, Fe, $Ni_{50}Fe_{50}$ and $Ni_{36}Fe_{64}$.

Electrochemical measurements. The measurements were carried out with an *Autolab potentiostat* in a standard three-electrode system using a GC disk, a Pt wire and a calomel electrode as a working, counter and reference electrode, respectively. All measured potentials were changed to the reversible hydrogen electrode (RHE) scale using the following equation: E (RHE) = E (SCE) + 0.242V+ 0.059×pH. The catalyst inks were deposited on the GC electrodes (0.19 cm^2) with the same loading of ~0.2 mg cm^{-2}. Subsequently, 25 µl of a 5 wt% Nafion dispersion was diluted with 1 ml of ethanol, and 5 µl of this solution was then added on top of the catalyst layers as a binder. Polarization curves were obtained using linear sweep voltammetry (LSV) with a scan rate of 5 mV s^{-1} in both 0.5 M H_2SO_4 and 0.1M NaOH electrolyte solutions. After the durability measurements, the electrolyte was changed to a fresh one before recording the HER activity. The uncompensated ohmic electrolyte resistance (R_u) was calculated by extrapolating R_u to the minimum total impedance in a non-Faradaic region, measured by impedance spectroscopy between 10 Hz and 100 kHz. The values of R_u ~ 6 Ω was recorded in 0.5 M H_2SO_4 solutions and R_u ~ 22 Ω was recorded in 0.1M NaOH solution.

X-ray photoelectron spectroscopy: X-ray photoelectron spectroscopy was performed using a Kratos Axis Ultra spectrometer with monochromated Al K_α radiation, using a pass energy of 40 eV and an X-ray power of 225 W. Samples were measured as powders dispersed on a gold foil except the sample characterized after the OER measurements which was measured directly on the glassy carbon electrode. The analysis area was roughly 700 µm × 300 µm for all samples. The binding energy scale

was referenced to the graphitic C 1s peak at 284.4 eV. The peak fitting of the nitrogen 1s region was done using Gaussian-Lorentzian peaks (70% Gaussian) with positions fixed to within ± 0.2 eV of given values and the full width at half maximum (FWHM) restricted to be equal. The N-oxide peak position was restricted to between 404 and 408 eV with the FWHM restricted to below 4 eV.

Raman studies. The Raman spectra were carried out using a JY LabRam 300 with 1.96 eV (633nm) laser excitation.

TEM analysis. For TEM characterization samples were dispersed in ethanol (~ 0.01 mg/ml) and then 10 µl of the solution drop cast on a carbon coated TEM grid (Cu grid) and dried in ambient air to form an ultra-thin film of the materials on the grid. All TEM images were obtained using a JEOL-2200FS, double Cs-corrected HRTEM at an acceleration voltage of 200 kV.

XRD measurement. For XRD measurements the samples were dried to obtain NP powders which were dispersed/spread/scattered onto Si-wafers. All measurements were conducted as GIXRD measurement with an PANalytical X'Pert Pro instrument within the 2Θ range of 25-100° and an overall measurement time of 2 hours.

X-ray Absorption Spectroscopy (XAS). X-ray absorption experiments were carried out using a low-cost laboratory X-ray absorption spectrometer designed for XAS

studies in the 4-20 keV photon energy range.[2,3] Experiments were performed at the Fe K-edge (7112 eV) and the Ni K-edge (8333 eV). The experimental setup consisted of a fixed Ag-tube as the X-ray source, with a moving bent Johan-type crystal monochromator and a moving NaI scintillator detector.[1] Samples were mounted to a sample exchanger positioned at the exit of the X-ray tube. Both powder references (Fe_2O_3, Fe_3O_4) and the nanoparticle samples were stored beforehand in an exicator and were measured in atmospheric conditions. For the experiments at the Fe K-edge, an X-ray tube acceleration voltage of 20 kV and a tube current of 4 mA was used. For the experiments at the Ni K-edge, the X-ray tube acceleration voltage was set to 10 kV and the current to 2 mA. Two different spherically bent crystal monochromators were employed: a Si (531) for the Fe K-edge measurements and a Si (551) for the Ni K-edge measurements. Both Si monochromators had a bending radius of 0.5 m. All obtained spectra were collected continuously in transmission mode and were calibrated and aligned using the corresponding Fe and Ni metal foils. Further details about the laboratory-based XAS setup and operation are found in the previous work.[2] The spectra were collected in a three-part scanning sequence. For the Fe K-edge measurements the scanning sequence was performed as follows: 7000 - 7089 eV (total of 101 points; 5 seconds per point), 7090 – 7190 eV (total of 201 points; 5 seconds per point), 7191 – 7280 eV (total of 101 points; 5 seconds per point). For the Ni K-edge measurements, the scanning sequence was performed as 8240 - 8319 eV (total of 80 points; 5 seconds per point), 8320 – 8420 eV (total of 201 points; 5 seconds per point), 8421 – 8510 eV (total of 90 points; 5 seconds per point). Data reduction and data analysis were performed using the ATHENA software package. Only the X-ray absorption near edge structure (XANES) analysis is presented in this work. Standard data for the Fe_3C, FeO, Ni_2O_3 and $Ni(OH)_2$ references were obtained from

the online XAFS Database. [4] For the Ni_3C [5,6] and NiO [6] references the standard data was extracted from the other works. [5,6]

In general, the spectrum produced due to metal K-edge XAS originates from electronic transitions of excited 1s electrons to either valence orbitals and/or into a continuum state. The produced spectrum has two distinct regions: an X-ray absorption near-edge structure (XANES) region, and an extended X-ray absorption fine structure (EXAFS) region. [7] In this work we are only focusing on the former region, and it comprises two distinguishable absorption features: a pre-edge absorption feature, assigned to 1s → 3d transitions, and an intense absorption edge, involving 1s → 4p transitions and/or 1s → 4p + ligand-to-metal charge transfer (LMCT) transitions. [7] To find the peak heights and positions of local maxima a "find local maxima peak" function in MATLAB was used.

Phase diagram calculation. The phase diagrams were calculated using MTDATA software[1] defining graphite as a present or dormant phase, thus allowing the stable and metastable phase equilibrium calculations, respectively, without further assumptions. The global boundary condition in the calculations was constant total pressure of 1 atm (101325.25 Pa).

Thermodynamic properties of Ni-Fe-C system are well known, and their solution properties have been critically assessed by several authors.[8,9] A dataset was defined containing carbon, iron and nickel as components, based on the internally consistent FeTC database [10] of Fe-based alloys of the MTDATA software. It allowed calculation of the detailed phase equilibria of carbon in Ni-Fe alloys and its distributions within the phases over a wide temperature range in solid and liquid systems.

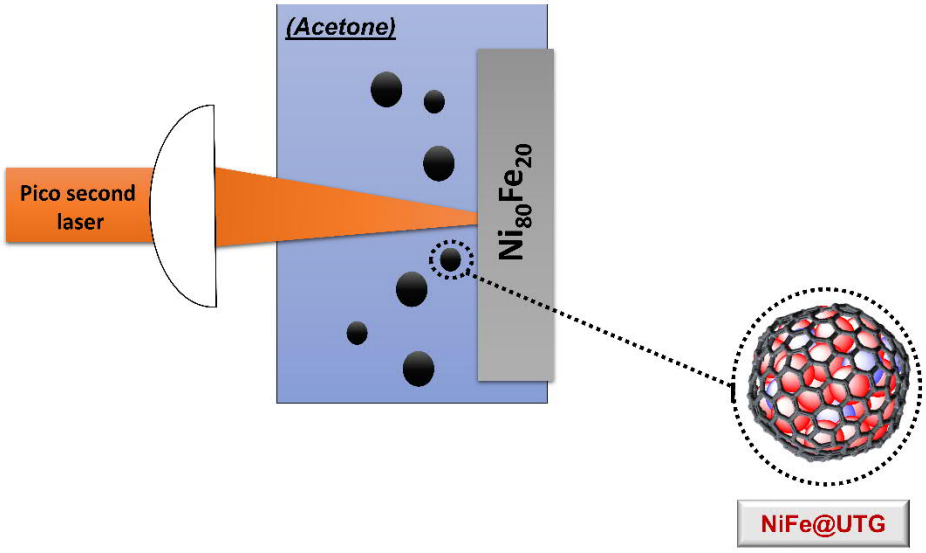

Figure 1. Scheme of the synthesis procedure of NiFe@UTG using a focused ps-laser in acetone via the PLAL method.

Scalability and overall cost of PLAL. Streubel et al. showed that by using high-power, high-repetition-rate ultrafast laser ablation in liquids nanoparticles can readily be prepared in continuous multigram scale [3] in form of pilot-scale synthesis [4]. The actual amount depends on the target material used [3,4]. They did not ablated $Ni_xFe_{(1-x)}$. However, they ablated Ni reaching productivities of about 2.5 g h^{-1}[4]. Besides the target material the productivity also depends on the solvent, being higher in water than in acetone [5].

Jendrzej et al. compared the synthesis of gold colloids by laser ablation in water and chemical reduction. They concluded that (in case of gold in water) the break even point of both methods is at a nanoparticle productivity of ≥550 mg h^{-1} where high power laser ablation starts to be more economical at industrial scale [6]. In case of the used $Ni_xFe_{(1-x)}$ the break even point will be different, but it is at least a study to see the potential of the method.

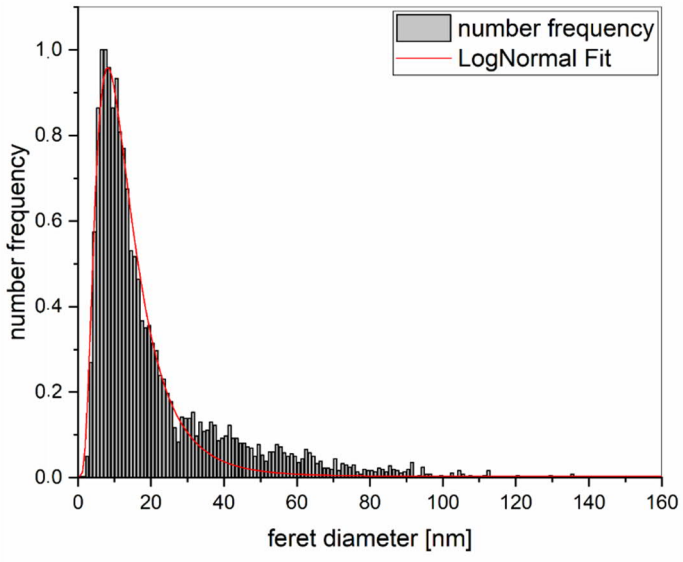

Figure S2. Size distributions of as-prepared NiFe@U 12.5 nm.

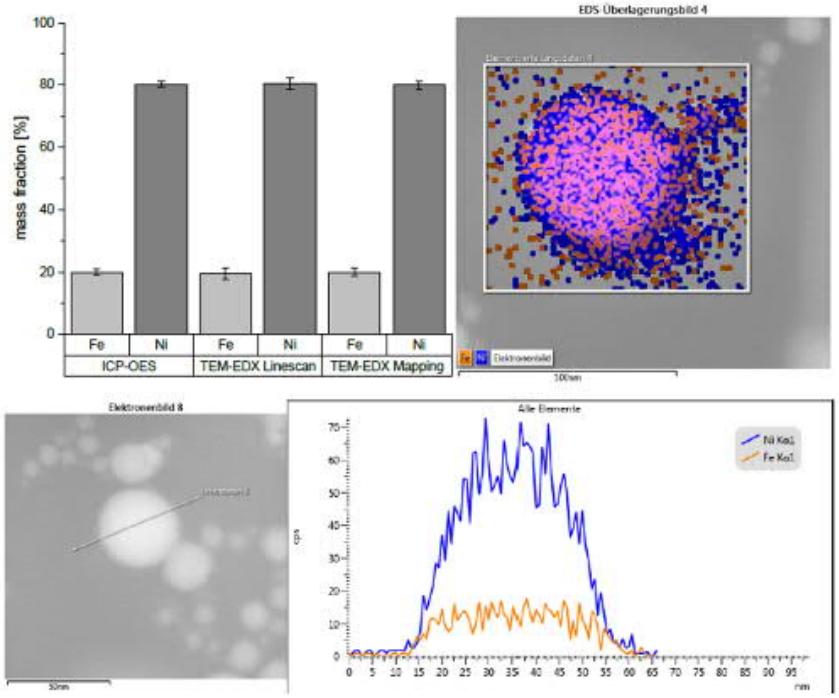

Figure S3. The elemental distribution within the colloid for $Ni_{80}Fe_{20}$ (NiFe@UTG) from TEM-EDX and ICP-OES.

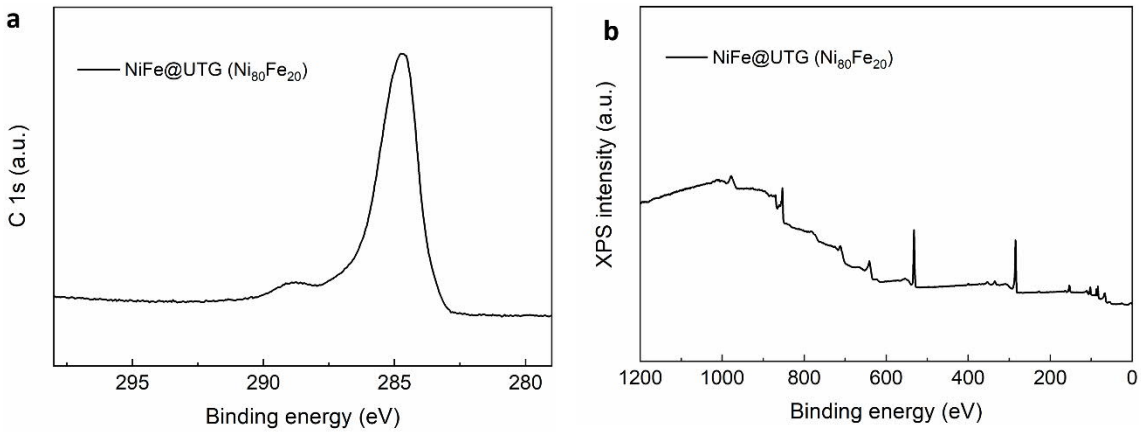

Figure S4. (a) C1s spectra and (b) X-ray Photoelectron Spectroscopy (XPS) survey spectra of sample NiFe@UTG.

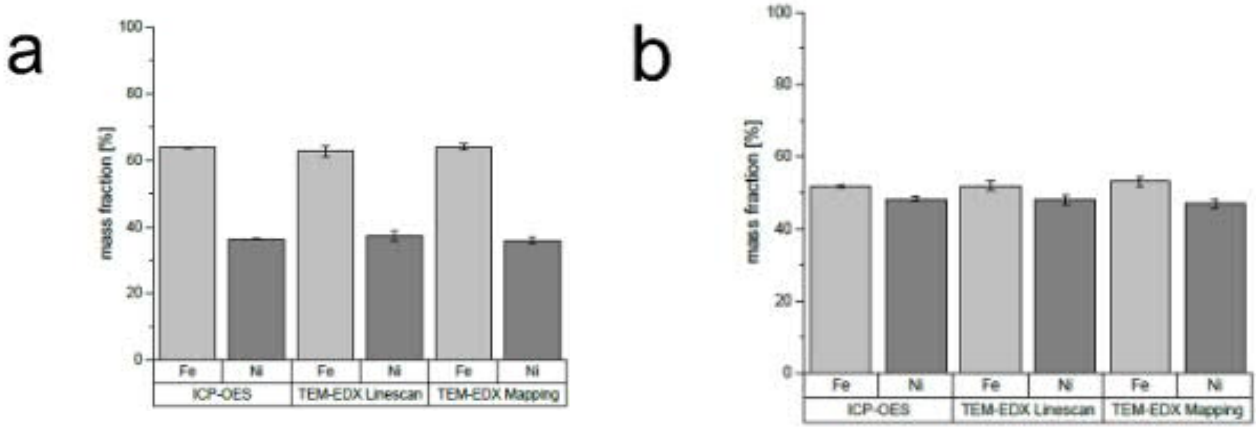

Figure S5. The elemental distribution within the colloid for **(a)** $Ni_{36}Fe_{64}$ and **(b)** $Ni_{50}Fe_{50}$ in acetone from TEM-EDX and an ICP-OES.

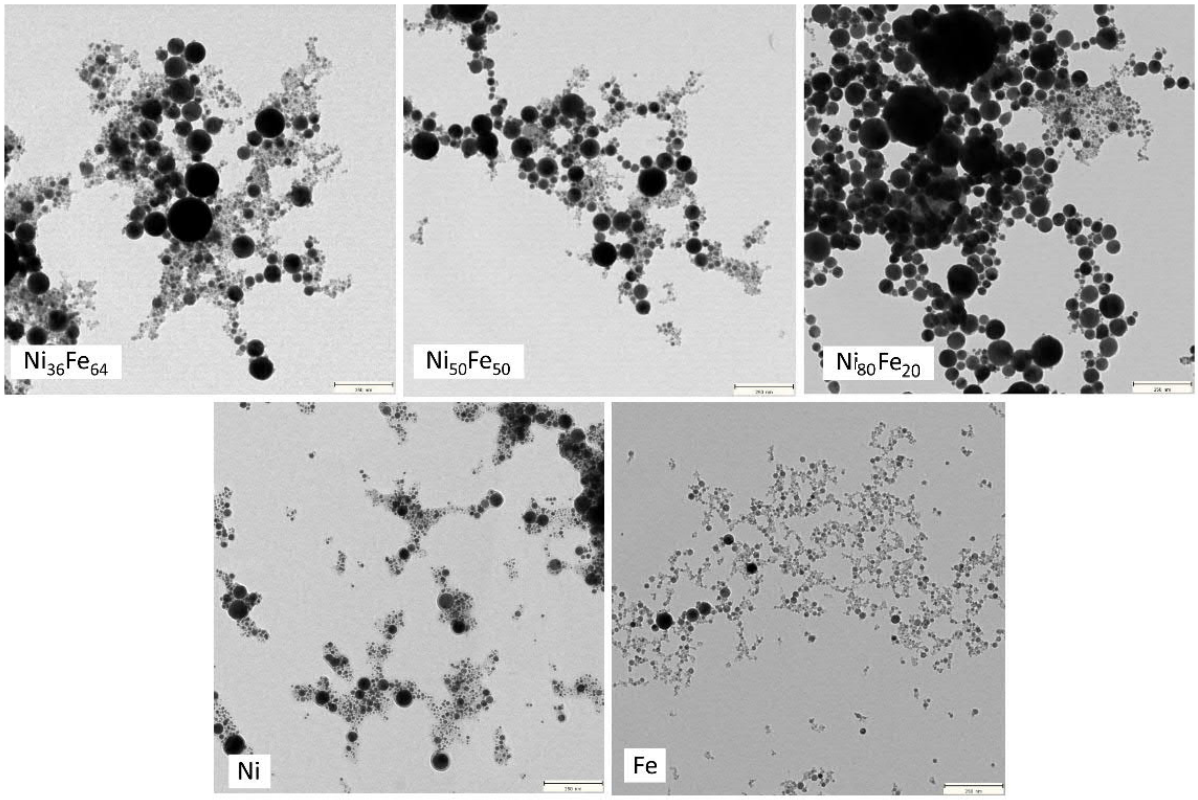

Figure S6. HRTEM images for different NPs formed in acetone. **(a)** $Ni_{36}Fe_{64}$, **(b)** $Ni_{50}Fe_{50}$, **(c)** $Ni_{80}Fe_{20}$ (NiFe@UTG), **(d)** Ni, and **(e)** Fe NPs.

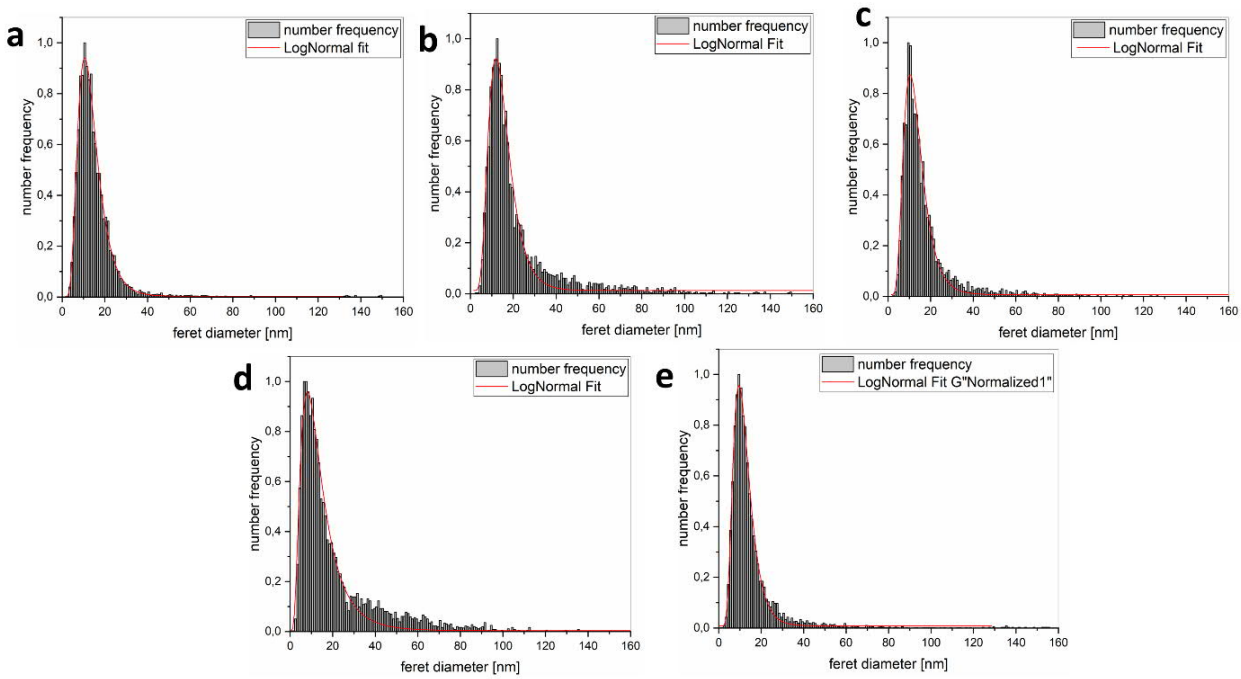

Figure S7. Size distributions of **(a)** Fe, **(b)** $Ni_{36}Fe_{64}$, **(c)** $Ni_{50}Fe_{50}$, **(d)** $Ni_{80}Fe_{20}$ (NiFe@UTG) and, **(e)** Ni NPs in acetone with ps-laser.

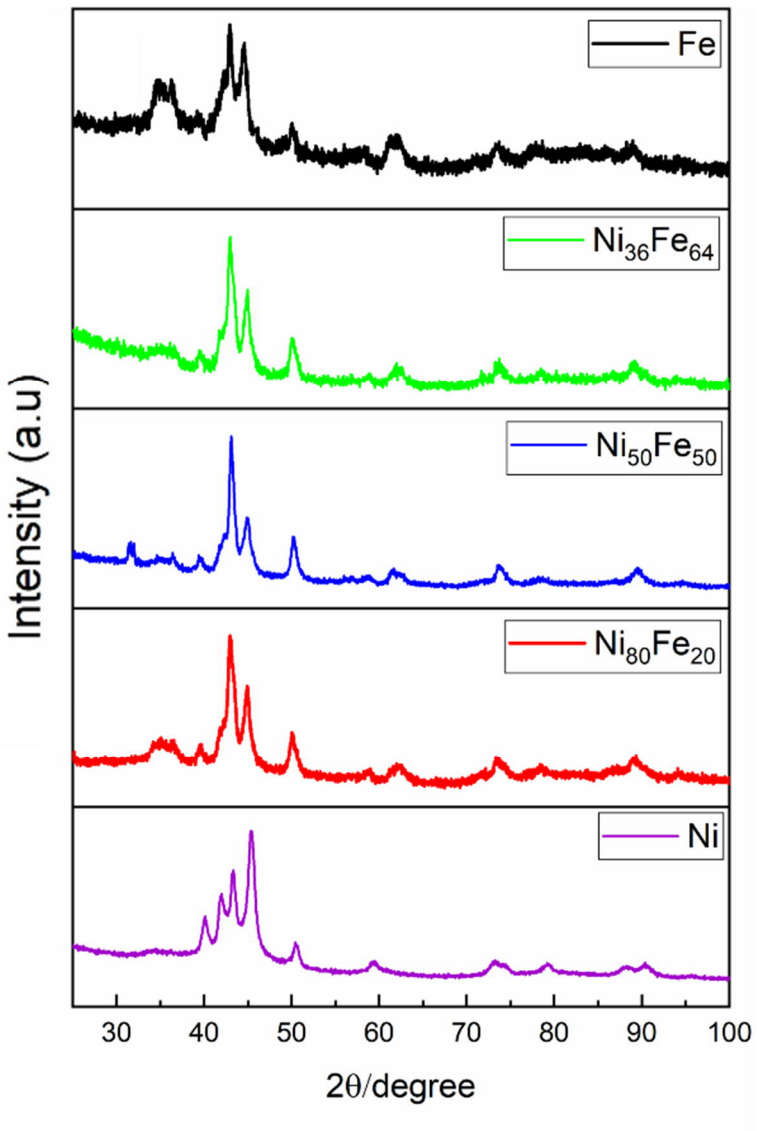

Figure S8. X-ray diffraction analysis of NPs with different Ni/Fe ratio.

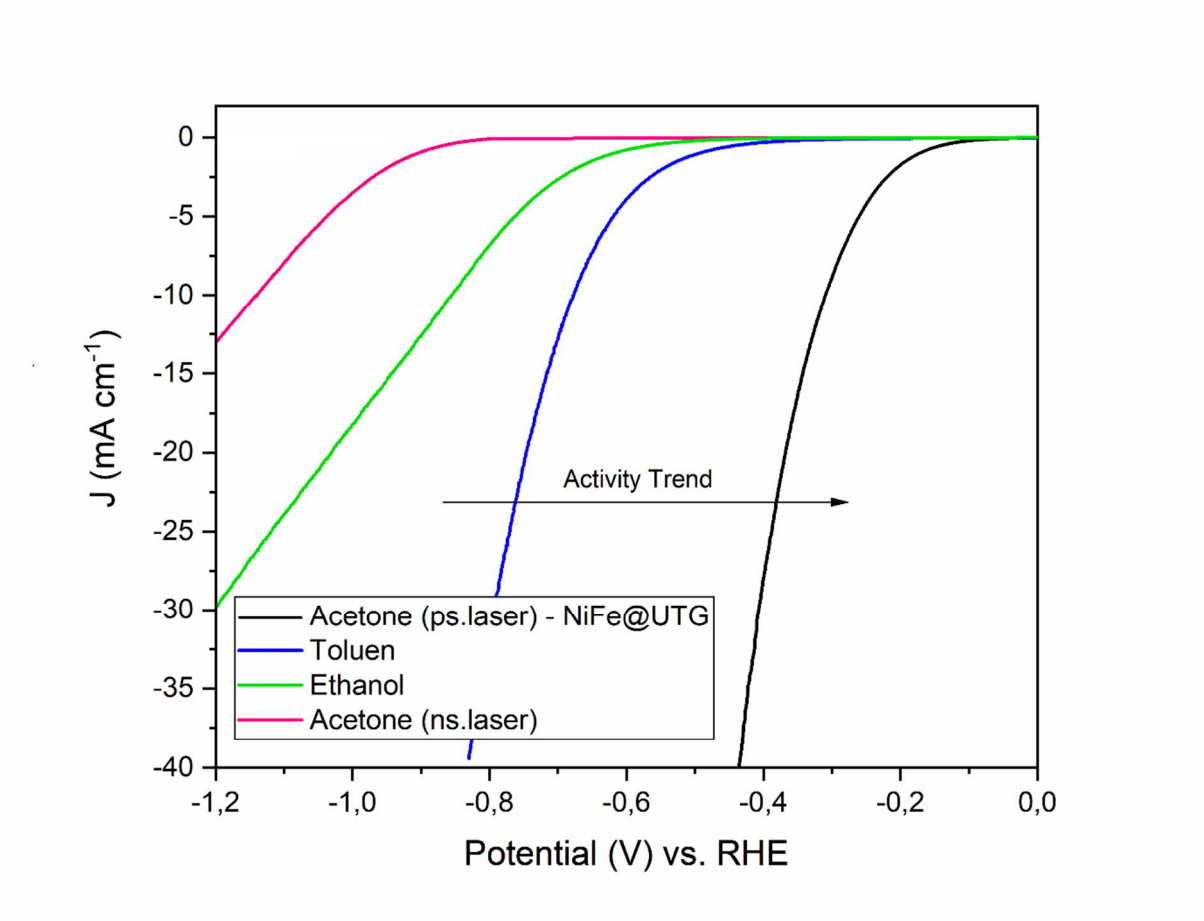

Figure S9. HER polarization curves for $Ni_{80}Fe_{20}$ NPs synthesized in different solutions and with different lasers.

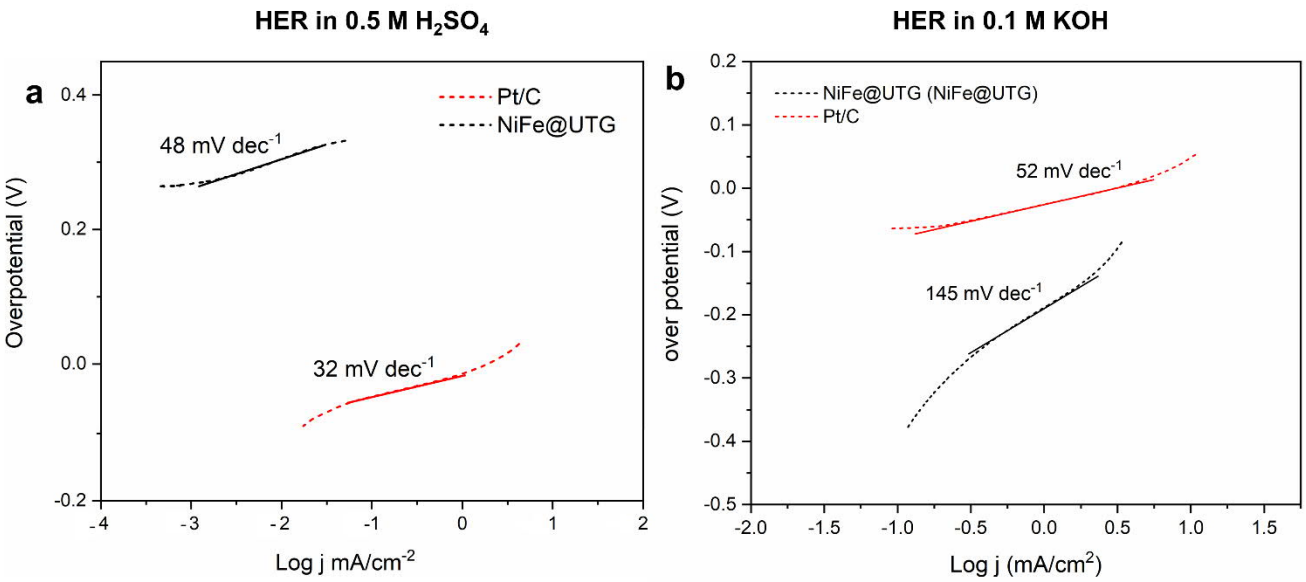

Figure S10. Tafel plotes aquired from polarization cure in Figure 9 for commercial Pt/C and NiFe@UTG ($Ni_{80}Fe_{20}$).

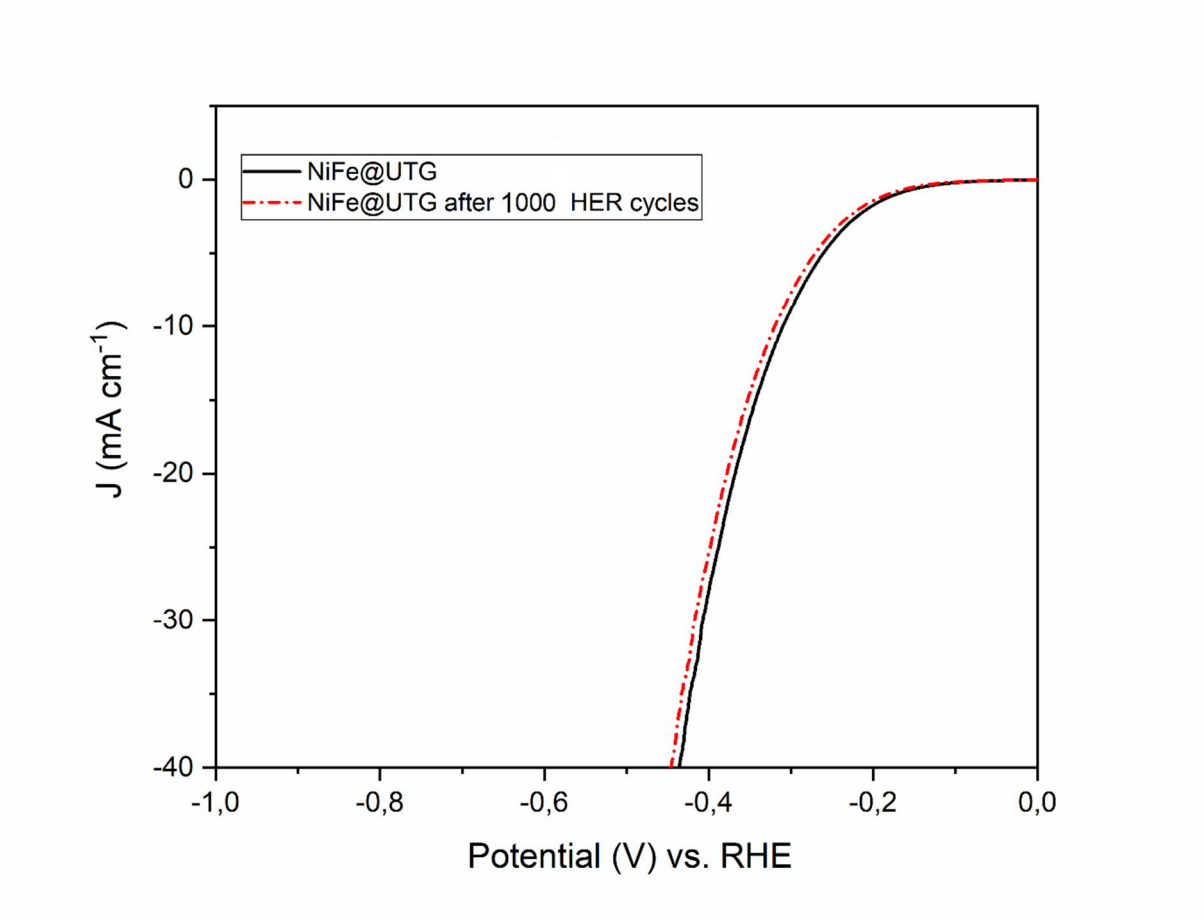

Figure S11. HER polarization curve for NiFe@UTG after 1000 HER cycles in 0.5 M H_2SO_4.

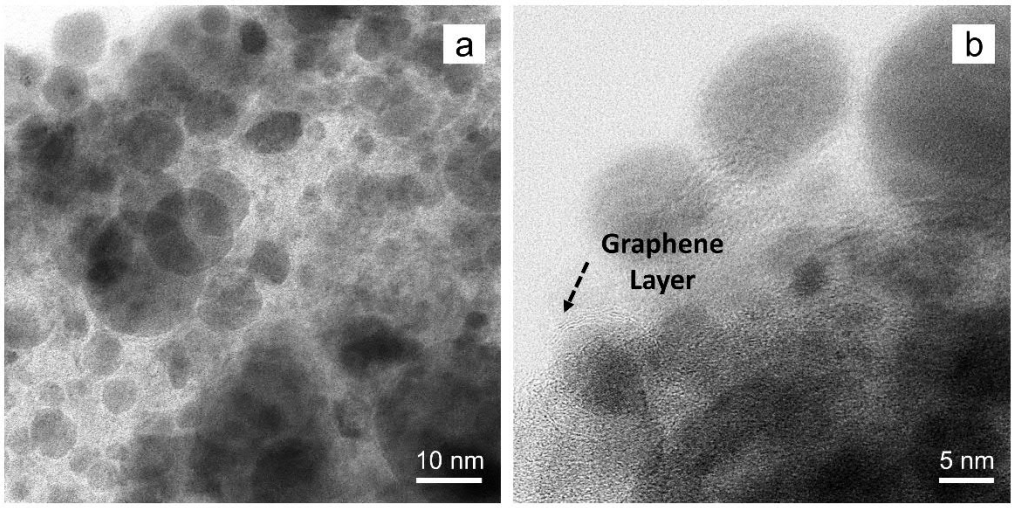

Figure S12. Morphology of the NiFe@UTG ($Ni_{80}Fe_{20}$) after long-term electrochemical measurements. HRTEM images show that NPs preserved their structures after long-term measurements.

Table S1. Fe Average Oxidation State Determination. Calculated Fe average oxidation state and energy positions of the half-height of the absorption edge feature in the normalized Fe K-edge XANES spectra. (E_0 = 7112 eV)

Half-height of the absorption edge					
Samples	**Calc. Fe AOS**	**Error**	**Energy Position (eV)**	**$\Delta E[E-E_0]$ (eV)**	**Error (eV)**
Std. Fe	0	0	7119.5	7.5	0.2
$Ni_{36}Fe_{64}$	1.4	0.1	7121.7	9.7	0.2
$Ni_{80}Fe_{20}$ (NiFe@ UTG)	1.5	0.1	7121.8	9.8	0.2
$Ni_{50}Fe_{50}$	1.6	0.1	7121.9	9.9	0.2
Fe	1.7	0.1	7122.0	10.0	0.2
Std. Fe_3O_4	2.67	0	7123.5	11.5	0.2
Std. Fe_2O_3	3	0	7124.0	12.0	0.2

Table S2. Comparison of HER performance of the NiFe@UTG catalyst to some of the state-of-the-art HER material, so far reported.

Catalysts	HER Onset overpotential (mV)	η_{HER10} (mV)	Catalyst loading (mg cm^{-2})	Electrolyte	Substrate	Ref.
NiFe@UTG	110	300	~0.2	0.5M H_2SO_4	GC	This work
NiFe@UTG	120	400	~0.2	0.1M KOH	GC	This work
NiFe@C	250	350	2	1M KOH	GC	[11]
FeCo@N-CNT	150	300	N/A	0.1M H_2SO_4	-	[12]
MoS_2 Ultrathin	180	220	0.25	0.5M H_2SO_4	GC	[13]
$[Mo_3S_{13}]^{2-}$ clusters on graphitic paper	100		~2×10^{-4}	0.5M H_2SO_4	GC	[14]
Exfoliated WS_2 nanosheets	80		~0.02	0.5M H_2SO_4	GC	[15]
Double- gyroid MoS_2	150-200		6.9×10^{-4}	0.5M H_2SO_4	GC	[16]
Mo_2C/CNT	-		0.014	0.5M H_2SO_4	GC	[17]
Mo_2C/CNT - graphene	62		0.062	0.5M H_2SO_4	GC	[18]
Nanoporous Mo_2C nanowires	70		-	0.5M H_2SO_4	GC	[19]
Core-shell MoO_3-MoS_2 Nanowires	150-200		~5.6×10^{-5}	0.5M H_2SO_4	GC	[20]
Exfoliated metallic MoS_2 nanosheets	~130		-	0.5M H_2SO_4	GC	[21]
MoS_2/ amorphous carbon	80		0.474	0.5M H_2SO_4	GC	[22]
MoO_2@N-doped MoS_2	156		-	0.5M H_2SO_4	GC	[23]
NiO_x/Pt–Ni	70 mV@19.8 mA cm^{-2}		N/A	1M KOH	GC	[24]
$Ni(OH)_2$–Pt/C	157 mV@5 mA cm^{-2}		N/A	0.1M KOH	GC	[25]
Pt–Ni/NiS	70 mV@37.2 mA cm^{-2}		N/A	1M KOH	GC	[26]
NiO/Ni-CNT	100 mV@10 mA cm^{-2}		N/A	1M KOH	GC	[27]
1T-MoS2/NiOOH	73 mV@10 mA cm^{-2}		N/A	1M KOH	GC	[28]
$MoSe_2$@$Ni_{0.85}Se$	117 mV@10 mA cm^{-2}		N/A	1M KOH	GC	[29]

References:

(1) Barcikowski, S.; Baranowski, T.; Durmus, Y.; Wiedwald, U.; Gökce, B. Solid Solution Magnetic FeNi Nanostrand–Polymer Composites by Connecting-Coarsening Assembly. *J. Mater. Chem. C* **2015**, *3* (41), 10699–10704. https://doi.org/10.1039/C5TC02160J.

(2) Honkanen, A.; Ollikkala, S.; Ahopelto, T.; Kallio, A.; Blomberg, M.; Huotari, S. Modes. **2019**, 1–10.

(3) I; Ari-Pekka Honkanen,[b] Ad M. J. van der Eerden,[a] Herrick Schaink, A.; Lieven Folkertsma,[a] Mahnaz Ghiasi,[a] Alessandro Longo,[c, D.; Frank M. F. de Groot, A.; Florian Meirer,[a] Simo Huotari, [b]; Weckhuysen*[a], and B. M. N□situ X□Ray Absorption Near Edge.Pdf. *ChemCatChem* **2019**, *11*, 1039–1044.

(4) Asakura, K. *Experimental Database XAFS as an Example*; 2018. https://doi.org/10.1107/S1600577518006963.Introduction.

(5) Struis, R. P. W. J.; Bachelin, D.; Ludwig, C.; Wokaun, A. Studying the Formation of Ni 3 C from CO and Metallic Ni at T) 265 ° C in Situ Using Ni K-Edge X-Ray Absorption Spectroscopy. **2009**, 2443–2451.

(6) Alsabban, B.; Falivene, L.; Kozlov, S. M.; Aguilar-tapia, A.; Ould-chikh, S.; Hazemann, J.; Cavallo, L.; Basset, J.; Takanabe, K. Applied Catalysis B : Environmental In-Operando Elucidation of Bimetallic CoNi Nanoparticles during High-Temperature CH 4 / CO 2 Reaction. *"Applied Catal. B, Environ.* **2017**, *213*, 177–189. https://doi.org/10.1016/j.apcatb.2017.04.076.

(7) Baker, M. L.; Mara, M. W.; Yan, J. J.; Hodgson, K. O.; Hedman, B.; Solomon, E. I. K- and L-Edge X-Ray Absorption Spectroscopy (XAS) and Resonant Inelastic X-Ray Scattering (RIXS) Determination of Differential Orbital Covalency (DOC) of Transition Metal Sites. *Coord. Chem. Rev.* **2017**, *345*, 182–208. https://doi.org/10.1016/j.ccr.2017.02.004.

(8) Natesan, K. Thermodynamics of Carbon in Nickel , Iron-Nickel and Iron-Chromium-Nickel Alloys. *Metall. Trans.* **1973**, *4* (November), 1973–2565.

(9) Gabriel, A.; Iq, M.; Gustafson, P. A Thermodynamic Evaluation of the C-Fe-Ni System. *Calphad* **1987**, *11* (2), 203–218.

(10) MTDATA.pdf http://resource.npl.co.uk/mtdata/downld_cust.htm.

(11) Park, S. W.; Kim, I.; Oh, S. I.; Kim, J. C.; Kim, D. W. Carbon-Encapsulated NiFe Nanoparticles as a Bifunctional Electrocatalyst for High-Efficiency Overall Water Splitting. *J. Catal.* **2018**, *366*, 266–274. https://doi.org/10.1016/j.jcat.2018.08.016.

(12) Deng, J.; Ren, P.; Deng, D.; Yu, L.; Yang, F.; Bao, X. Highly Active and Durable Non-Precious-Metal Catalysts Encapsulated in Carbon Nanotubes for Hydrogen Evolution Reaction. *Energy Environ. Sci.* **2014**, *7* (6), 1919. https://doi.org/10.1039/c4ee00370e.

(13) Xie, J.; Zhang, H.; Li, S.; Wang, R.; Sun, X.; Zhou, M.; Zhou, J.; Wen, X.; Lou, D.; Xie, Y. Defect-Rich MoS 2 Ultrathin Nanosheets with Additional Active Edge Sites for Enhanced Electrocatalytic Hydrogen Evolution. **2013**, 5807–5813. https://doi.org/10.1002/adma.201302685.

(14) Kibsgaard, J.; Jaramillo, T. F.; Besenbacher, F. Building an Appropriate Active-

Site Motif into a Hydrogen-Evolution Catalyst with Thiomolybdate [Mo3S13]2- Clusters. *Nat. Chem.* **2014**, *6* (3), 248–253. https://doi.org/10.1038/nchem.1853.

(15) Voiry, D.; Yamaguchi, H.; Li, J.; Silva, R.; Alves, D. C. B.; Fujita, T.; Chen, M.; Asefa, T.; Shenoy, V. B.; Eda, G.; et al. Enhanced Catalytic Activity in Strained Chemically Exfoliated WS 2 Nanosheets for Hydrogen Evolution. *Nat. Mater.* **2013**, *12* (9), 850–855. https://doi.org/10.1038/nmat3700.

(16) Kibsgaard, J.; Chen, Z.; Reinecke, B. N.; Jaramillo, T. F. Engineering the Surface Structure of MoS 2 ToÂ Preferentially Expose Active Edge Sites ForÂ Electrocatalysis. *Nat. Mater.* **2012**, *11* (11), 963–969. https://doi.org/10.1038/nmat3439.

(17) Chen, W. F.; Wang, C. H.; Sasaki, K.; Marinkovic, N.; Xu, W.; Muckerman, J. T.; Zhu, Y.; Adzic, R. R. Highly Active and Durable Nanostructured Molybdenum Carbide Electrocatalysts for Hydrogen Production. *Energy Environ. Sci.* **2013**, *6* (3), 943–951. https://doi.org/10.1039/c2ee23891h.

(18) Youn, D. H.; Han, S.; Kim, J. Y.; Kim, J. Y.; Park, H.; Choi, S. H.; Lee, J. S. Highly Active and Stable Hydrogen Evolution Electrocatalysts Based on Molybdenum Compounds on Carbon Nanotube-Graphene Hybrid Support. *ACS Nano* **2014**, *8* (5), 5164–5173. https://doi.org/10.1021/nn5012144.

(19) Liao, L.; Wang, S.; Xiao, J.; Bian, X.; Zhang, Y.; Scanlon, M. D.; Hu, X.; Tang, Y.; Liu, B.; Girault, H. H. A Nanoporous Molybdenum Carbide Nanowire as an Electrocatalyst for Hydrogen Evolution Reaction. *Energy Environ. Sci.* **2014**, *7* (1), 387–392. https://doi.org/10.1039/c3ee42441c.

(20) Chen, Z.; Cummins, D.; Reinecke, B. N.; Clark, E.; Sunkara, M. K.; Jaramillo,

T. F. Core-Shell MoO3-MoS2 Nanowires for Hydrogen Evolution: A Functional Design for Electrocatalytic Materials. *Nano Lett.* **2011**, *11* (10), 4168–4175. https://doi.org/10.1021/nl2020476.

(21) Lukowski, M. A.; Daniel, A. S.; Meng, F.; Forticaux, A.; Li, L.; Jin, S. Enhanced Hydrogen Evolution Catalysis from Chemically Exfoliated Metallic MoS2 Nanosheets. *J. Am. Chem. Soc.* **2013**, *135* (28), 10274–10277. https://doi.org/10.1021/ja404523s.

(22) Zhao, X.; Zhu, H.; Yang, X. Amorphous Carbon Supported MoS 2 Nanosheets as Effective Catalysts for Electrocatalytic Hydrogen Evolution. *Nanoscale* **2014**, *6* (18), 10680–10685. https://doi.org/10.1039/c4nr01885k.

(23) Zhou, W.; Hou, D.; Sang, Y.; Yao, S.; Zhou, J.; Li, G.; Li, L.; Liu, H.; Chen, S. MoO2 Nanobelts@nitrogen Self-Doped MoS2 Nanosheets as Effective Electrocatalysts for Hydrogen Evolution Reaction. *J. Mater. Chem. A* **2014**, *2* (29), 11358–11364. https://doi.org/10.1039/c4ta01898b.

(24) Wang, P.; Jiang, K.; Wang, G.; Yao, J.; Huang, X. Phase and Interface Engineering of Platinum–Nickel Nanowires for Efficient Electrochemical Hydrogen Evolution. *Angew. Chemie - Int. Ed.* **2016**, *55* (41), 12859–12863. https://doi.org/10.1002/anie.201606290.

(25) Wang, L.; Lin, C.; Huang, D.; Chen, J.; Jiang, L.; Wang, M.; Chi, L.; Shi, L.; Jin, J. Optimizing the Volmer Step by Single-Layer Nickel Hydroxide Nanosheets in Hydrogen Evolution Reaction of Platinum. *ACS Catal.* **2015**, *5* (6), 3801–3806. https://doi.org/10.1021/cs501835c.

(26) Wang, P.; Zhang, X.; Zhang, J.; Wan, S.; Guo, S.; Lu, G.; Yao, J.; Huang, X. Precise Tuning in Platinum-Nickel/Nickel Sulfide Interface Nanowires for

Synergistic Hydrogen Evolution Catalysis. *Nat. Commun.* **2017**, *8*, 1–9. https://doi.org/10.1038/ncomms14580.

(27) Xu, J.; Liu, T.; Li, J.; Li, B.; Liu, Y.; Zhang, B.; Xiong, D.; Amorim, I.; Li, W.; Liu, L. Boosting the Hydrogen Evolution Performance of Ruthenium Clusters through Synergistic Coupling with Cobalt Phosphide. *Energy Environ. Sci.* **2018**, *11* (7), 1819–1827. https://doi.org/10.1039/c7ee03603e.

(28) Zhang, X.; Liang, Y. Nickel Hydr(Oxy)Oxide Nanoparticles on Metallic MoS 2 Nanosheets: A Synergistic Electrocatalyst for Hydrogen Evolution Reaction. *Adv. Sci.* **2018**, *5* (2). https://doi.org/10.1002/advs.201700644.

(29) Wang, C.; Zhang, P.; Lei, J.; Dong, W.; Wang, J. Integrated 3D MoSe 2 @Ni 0.85 Se Nanowire Network with Synergistic Cooperation as Highly Efficient Electrocatalysts for Hydrogen Evolution Reaction in Alkaline Medium. *Electrochim. Acta* **2017**, *246*, 712–719. https://doi.org/10.1016/j.electacta.2017.06.028.